

Dual Emission of Water-Stable 2D Organic–Inorganic Halide Perovskites with Mn(II) Dopant

Qiankai Ba, Atanu Jana, Lihua Wang, and Kwang S. Kim*

Moisture-delicate and water-unstable organic–inorganic halide perovskites (OI-HPs) create huge challenges for the synthesis of highly efficient water-stable light-emitting materials for optoelectronic devices. Herein, a simple acid solution–assisted method to synthesize quantum confined 2D lead perovskites through Mn doping is reported. The efficient energy transfer between host and dopant ions in orange light-emitting Mn²⁺-doped OI-HPs leads to the most efficient integrated luminescence with a photoluminescence quantum yield over 45%. The Mn²⁺ substitution of Pb²⁺ and passivation with low dielectric constant molecules such as phenethylamine, benzylamine, and butylamine enhance water resistivity, leading to water stability. The dual emission process of this water-stable 2D Mn-doped perovskite will help in developing highly efficient 2D water-stable perovskites for practical applications.

1. Introduction

Low-dimensional lead halide perovskites have received great attention for the performance improvement of solar cells, lasers, light-emitting diodes (LEDs), and high-gain photodetectors due to their excellent optical performance.^[1–3] In particular, halide perovskite-based LEDs have shown exciting prospects.^[4] Along with the rapid development of display technologies, the next-generation flexible emitters with high color purity and low fabrication cost are highly demandable. The low-dimensional organic–inorganic halide perovskites (OI-HPs) have recently emerged as an alternative to 3D perovskites^[5–10] due to their easily tunable band-edge emission, high color purity, high photoluminescence quantum yield (PL-QY), improved moisture resistance, and thermostability. Unfortunately, compared with the rapid development of all inorganic lead halide perovskites which have archived the highest external quantum efficiency (EQE) of 20.3%,^[4] the development pace of the low-dimensional OI-HP with the general formula A₂A''_{n-1}BX_{3n+1}, despite the strong merit of large surface area, has significantly lagged with the EQE of 14.46%.^[11] Most critical drawbacks of the low-dimensional halide perovskite materials are attributed to their

instability against water and dielectric organic capping layer. Further development should be achieved so as to obtain the efficiencies on par with their bulk 3D counterparts.

In general, 3D ABX₃ perovskites tend to hydrolyze in presence of water, resulting in destruction of the lattice structure.^[12] As 2D perovskites show a higher structure tolerance factor than 3D ones, great efforts have been made to achieve highly moisture-stable perovskites with excellent device performance in lower dimensions.^[13–15] Main approaches to suppress this moisture-driven degradation process are to control the capping layers and anion compositions.^[14–19] By incorporating these large-sized molecules into

3D APbX₃ to form the A'₂A_{n-1}B_nX_{3n+1} structure, the thickness of the perovskite can be controlled as small as $n = 1$. Sargent and co-workers^[15] reported a series of dimension-controlled quasi-2D perovskites by inducing hydrophobic phenethylamine (PEA) molecules as a partial substitution for MAs in MAPbBr₃. This procedure enhanced the stability of 2D perovskites. Moreover, through controlling the coordination interaction, the stability of perovskite materials can also be improved similarly by introducing SCN functional groups as a partial substituent for anions.^[16,17] Although these methods are cost-effective for stabilizing perovskite materials, the core challenges to improve the efficiencies of perovskites are still urged to be made.

Although the organic molecular capping becomes an efficient way to enhance water resistance to perovskite materials, it also creates a dielectric layer impeding the efficient carrier injection. Therefore, 2D perovskite LEDs suffer from low quantum efficiency. Recently, efforts have been made to balance the adverse effects induced by organic capping group through doping. Mn-doped perovskites are receiving much attention since the first Mn-doped CsPbCl₃ was reported in 2016.^[20] Mn²⁺ doping in semiconductor nanocrystals is widely known for its long lifetime of Mn d–d orange emission and the efficient exciton energy transfer between semiconductor host and Mn²⁺ dopant. Subsequently, high PL-QYs of thermostability-enhanced all-inorganic CsPbX₃ materials were reported in succession.^[21–23] Further exploration of Mn²⁺-doped perovskite has also been extended to OIHPs.^[23–25] However, there is no report on water-stable Mn-doped perovskite nanocrystals.

Here, we demonstrate that the B site dopant and the proper steric arrangement of A site stabilize 2D OI-HP crystals in water and improve optical performance due to the enhanced quantum and dielectric confinement effects. We develop a

Q. Ba, Dr. A. Jana, Dr. L. Wang, Prof. K. S. Kim
Center for Superfunctional Materials
Department of Chemistry
Ulsan National Institute of Science and Technology (UNIST)
Ulsan 44919, South Korea
E-mail: kimks@unist.ac.kr

 The ORCID identification number(s) for the author(s) of this article can be found under <https://doi.org/10.1002/adfm.201904768>.

DOI: 10.1002/adfm.201904768

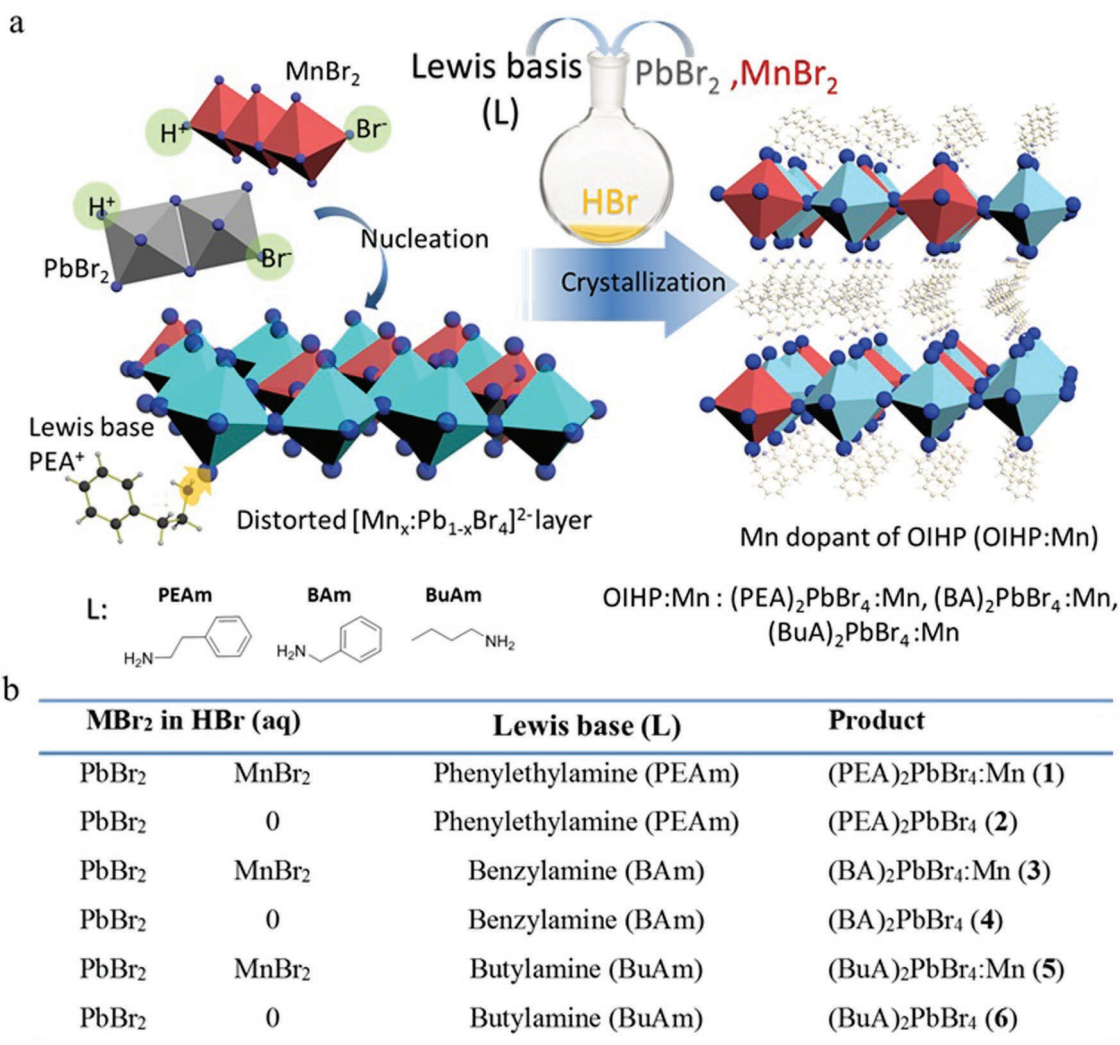


Figure 1. a) Schematic illustration of water-stable 2D OI-HP:Mn through ALBP method and the chemical structures of phenylethylamine, benzylamine, and butylamine, and chemical component of Mn-doped 2D OI-HPs: $(\text{PEA})_2\text{PbBr}_4:\text{Mn}$ (1), $(\text{BA})_2\text{PbBr}_4:\text{Mn}$ (2), and $(\text{BuA})_2\text{PbBr}_4:\text{Mn}$ (3). b) List of all synthesized compounds from their precursor materials and the structural formulas.

simple and performant route to synthesize pure and Mn-doped 2D OI-HPs (2D OI-HP:Mn) through acid solution-assisted Lewis-base precipitating method: $(\text{PEA})_2\text{PbBr}_4:\text{Mn}$ (1), $(\text{BA})_2\text{PbBr}_4:\text{Mn}$ (3), $(\text{BuA})_2\text{PbBr}_4:\text{Mn}$ (5), $(\text{PEA})_2\text{PbBr}_4$ (2), $(\text{BA})_2\text{PbBr}_4$ (4), and $(\text{BuA})_2\text{PbBr}_4$ (6). Unlike commonly used synthesis strategies, we dissolve PbBr_2 and MnBr_2 in hydrobromic acid solution followed by injecting into Lewis base to precipitate perovskite crystals under sonification. We obtain disk-like perovskite nanoplates of 1–6. By comparing different organic cations, we achieve the highest solid-state PL-QY exceeding 45% for 1. We assign it to a dual emission process resulting from 2D perovskite band-edge absorption, energy transfer between semiconductor host and Mn^{2+} , and absorption from $\text{Mn}^{2+} {}^4\text{T}_1\text{--}{}^6\text{A}_1$ ligand-field band in the 2D OI-HP:Mn system. Furthermore, Mn-doped perovskite nanocrystals 1 show the long-term water-stable fluorescence, while 3 and 5 decompose quickly in water. We demonstrate that the proper steric hydrophobic π -conjugated PEA molecules and

Mn^{2+} dopants enhance the water stability of 2D OI-HP. We demonstrate, for the first time, that the high fluorescence of Mn-doped $(\text{PEA})_2\text{PbBr}_4$ nanocrystal can be stabilized in water over 45 days. We believe that our findings will pave the practical applications of new highly stable 2D perovskite with prolonged high-performance perovskite LEDs and luminescent indicators.

2. Results and Discussion

2D OI-HP and 2D OI-HP:Mn crystals are synthesized, following the acid-assisted Lewis-base precipitating method according to a previously reported method with some modification.^[19,26] In a typical synthesis, PbBr_2 and MnBr_2 with different ratios were dissolved individually in HBr in a 25 mL one-neck bottle under sonication (Figure 1). Lewis bases were added into the solution of metal halide precursor one at a time to precipitate the tawny solid. In the case of post-treatment of the compounds,

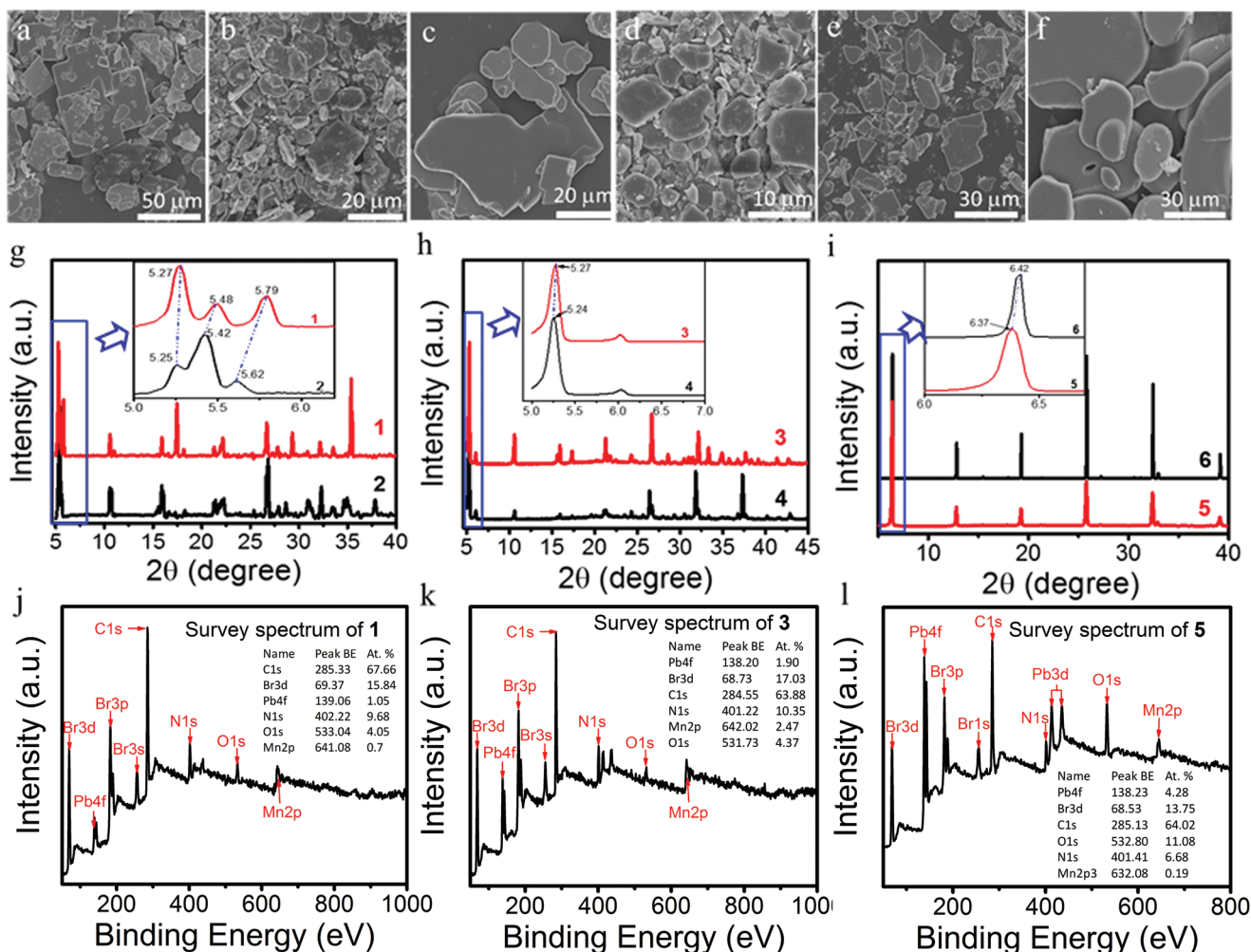


Figure 2. SEM images for a) 1, b) 3, c) 5, d) 2, e) 4, and f) 6 and their corresponding XRD patterns for g) 1, h) 3, and i) 5, showing that all XRD peaks can be indexed compared with their undoped compounds as well as the XPS survey spectra recorded on j) 1, k) 3, and l) 5, respectively.

we isolated the precipitate and washed the solid with water to remove the acid solution several times, and dried them at 60 °C in an oven for overnight to obtain yellowish white powder. The dried samples exhibited bright reddish-orange fluorescence under 365 nm UV light. At the same time only nanocrystals 1 show ultrastability in water (as shown in the video in the Supporting Information). The detailed synthesis information of all compounds is given in the Experimental Section.

2.1. Structure Characterization of the Mn-Doped 2D Structure

All the samples are first examined by high-power X-ray diffraction (HP-XRD) measurement and scanning electronic microscopy (SEM) to verify the crystal structures and morphology, respectively (Figure 2; Figure S1, Supporting Information). As illustrated in a previous report,^[27] dopant ions tend to occupy the position of Pb^{2+} without accumulating in interstices because of the low formation energy when crystallized from precursors. In Figure 2g–i, XRD analyses were performed for Mn-doped 2D OI-HPs (1, 3, 5) and the intrinsic un-doped 2D OI-HPs (2,

4, 6). More careful examinations were made in magnified views in Figure 2. From the XRD patterns, the appearance of peaks at similar positions reveal that 2D OI-HP:Mn was inherited from its layered structure type.^[28] The structure was further confirmed to have the plate/disk shaped morphology from SEM images (Figure 2a–f). Although the thicknesses were much more than a single layer of perovskite, it is likely to be attributed to their self-organization among layers.^[29] The constituent elements were confirmed through SEM/EDS analysis (Figures S2–S13, Supporting Information). We randomly selected three particles for SEM/EDS and the composition analyses were made (Table S1, Supporting Information). The SEM-EDX measurements show that in these particles the atom molar ratios of Pb/Mn are 1.55, 0.88, and 1.16. Representative transmission electron microscopy (TEM) images in Figure S1 (Supporting Information) show the perovskite lattice fringes corresponding to the well-indexed 2D perovskite. The dominance of the (00l) peaks in the XRD pattern demonstrate the highly oriented crystal structure in the direction of the c-axis being perpendicular to the layer plane.^[30] Furthermore, the small diffraction angles below 10° indicate the (002) lattice plane which forms

the 2D layered structure, consistent with the interlayer spacing calculated from XRD patterns.^[31] The *d*-spacings for 1, 3, and 5, consisting of single inorganic octahedra layer and organic ligands layer, are 1.67, 1.67, and 1.375 nm, respectively.^[32] Klimov and co-workers demonstrated that alloy formation gives X-ray diffraction peaks at higher 2θ -values.^[21] For Mn-doped perovskite, the Mn^{2+} ion preferably incorporates with bromide atoms and occupies the substitution position during perovskite nanocrystal formation.^[33] As a result, Mn^{2+} dopant shows monotonical shift to higher angles as compared to the undoped perovskite. As shown in the magnified views in Figure 1 and Figure S1 (Supporting Information), all the XRD patterns shifts to higher angles, in good consistency with previous reports, give clear evidence for Mn doping.

To further verify the conclusion drawn from the SEM/EDS and XRD pattern, XPS comparative analyses between 2D OI-HP:Mn and undoped perovskites were performed (Figure 2j–l, Figures S14–S16, Supporting Information). The results reveal that both undoped and Mn-doped 2D OI-HPs comprise the C, N, O, Pb, and Br elements. The existence of Mn was also proven from the XPS spectra for 1, 3, and 5. To further confirm the detailed element information, we conducted high-resolution XPS spectroscopy of all elements for 2D OI-HP:Mn (Figures S14–S16, Supporting Information). The chemical composition analysis was shown in Figure 2j–l. We found that these atomic ratios of Pb:Mn (1.5 and 0.77 for 1 and 3, respectively) are nearly consistent with chemical composition results presented by SEM/EDS for 1 and 3. The comparative results give an evidence for dopant atoms incorporated successfully in the lattice rather than bounded to nanoplate surface. In

Figures S14–S16 (Supporting Information), the high-resolution XPS spectra of Pb element demonstrated that the bonding energy of $\text{Pb}^{2+} 4f_{5/2}$ and $\text{Pb}^{2+} 4f_{7/2}$ nearly retained the same when Mn^{2+} ions were introduced into the 2D OI-HP lattice structure.^[34] The binding energy peaks of Mn derivatives and O1s were presented in all the doped compounds. This is the signature for formation of the manganese oxides and lead oxide derivatives on the surface of the disk crystals due to partial oxidation during exposing in air.

2.2. Optical Properties of Undoped and Mn-Doped 2D OI-HPs

The optical characterizations of 2D OI-HP and Mn^{2+} incorporated 2D OI-HP were performed using ultraviolet–visible light (UV–vis) absorption spectroscopy and PL spectroscopy. Mn^{2+} known as an efficient luminescent activator usually gives rise to spectacular PL properties in doped semiconductors. The PL emission originates from band-edge emission and Mn^{2+} emission,^[21,35–37] which are attributed to the 2D OI-HP intrinsic free excitonic recombination and bound excitonic recombination, respectively.^[21,38] The spectra in Figure 3 show the room-temperature PL features and UV–vis absorption features of 2D perovskite 1–6. The pure 2D OI-HPs presented the characteristic emission peak for layered perovskite at 420, 417, and 427 nm for 2, 4, and 6, respectively. However, 1, 3, and 5 showed multiemission peaks with narrow emission at nearly 417 nm and broad emission between 550 and 700 nm. The narrow sharp peaks at nearly 417 nm are the intrinsic 2D OI-HP excitonic PL, and the broad emission peaks centered at

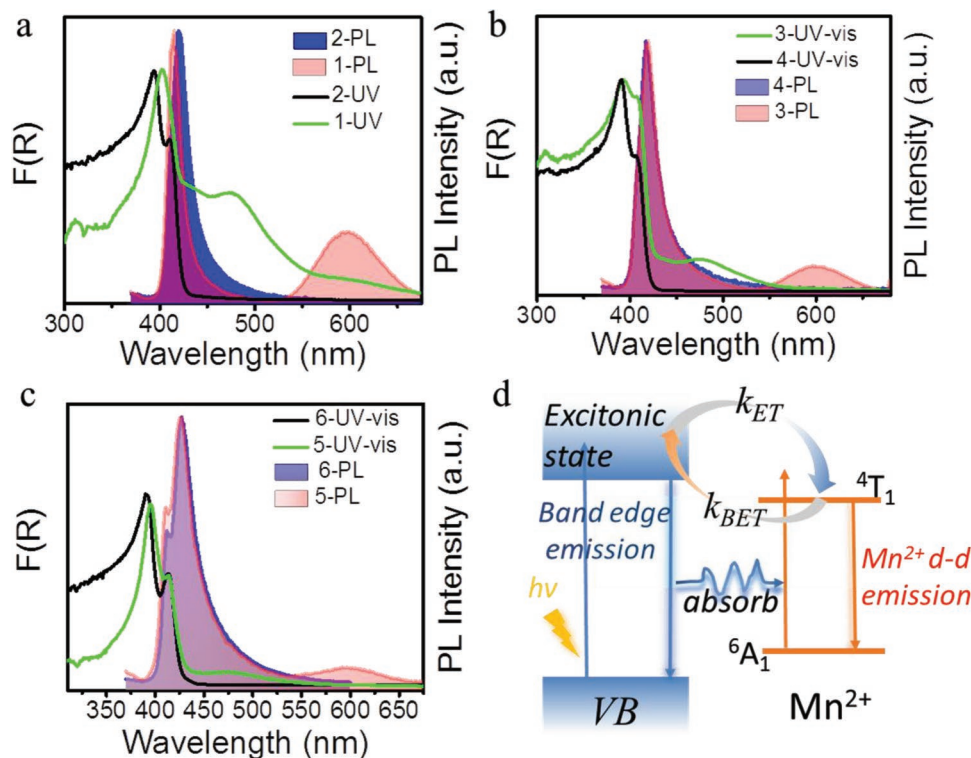


Figure 3. Room-temperature absorption PL spectra for a) UV–vis and PL of 2 and 1, b) UV–vis and PL of 4 and 3, and c) UV–vis and PL of 6 and 5, and d) schematic illustration of energy transfer for Mn-dopant system. ET: energy transfer; BET: back energy transfer.

600 nm are $\text{Mn}^{2+} \ ^4\text{T}_1\text{-}^6\text{A}_1$ transitions.^[38] The absorption spectra are characterized by band-edge absorption and $\text{Mn}^{2+} \ ^4\text{T}_1\text{-}^6\text{A}_1$ ligand-field band absorption. In previous reports,^[21,22,39] $\text{Mn}^{2+} \ ^4\text{T}_1\text{-}^6\text{A}_1$ transition dominates the orange fluorescence at room temperature in Mn-doped perovskites, accompanied by minor change in absorption spectra between 2D OI-HP and doped 2D OI-HP. Mn dopants give a weak effect on the electronic structure of the host nanocrystals due to the spin forbidden nature of the transition. Notably, we found that 2D OI-HP:Mn (**1**, **3**, and **5**) features the absorption spectra extending to nearly 600 nm from 350 nm, which shows a significant change from their host semiconductors. We observed a new absorbance peak in Mn-doped compound **1**. The new peak may appear due to the formation of cluster that could enhance the scattering phenomenon during absorbance measurement. It should be mentioned that absorbance is sensitive to the morphology of materials. But we ruled out the scattering phenomenon by micro-UV-vis analysis and confirmed that the new absorption band for the Mn-doped materials stems from Mn^{2+} doping. We have taken the micro-UV-vis spectra to investigate the single nanoplate absorption properties (Figure S21, Supporting Information) and we compare the absorption of powder with single nanoplate for perovskite **1**. A semblable absorption transition was observed. As the formation of clusters, the absorption of powder exhibits the spectrum extended to 650 nm. It is illustrated by the nearly coincident spectra in the range 450–650 nm. We reveal that the new absorption band is attributed to the absorptions of band-edge transition and lowest-energy ligand field transitions of Mn^{2+} ($^6\text{A}_1 \rightarrow ^4\text{T}_1$) (Figure 3a–d).^[23,38]

Indeed, substituent of Pb^{2+} (138 pm) with smaller radius of Mn^{2+} (67 pm) will lead to enhanced interaction between B site ions and Br^- ion.^[22] Meanwhile, the organic linkers have smaller dielectric constant and favor increased dielectric confinement effects of 2D perovskites and even inherent intrinsic quantum confinement properties of 2D perovskites.^[40,41] As a result, intrinsic quantum and dielectric confinement effects greatly act on large exciton binding energies associated with the unusual optoelectronic properties of low-dimensional perovskites.^[41,42] **Table 1** lists composition data and optical properties for 2D OI-HP:Mn (**1**, **3**, and **5**) and 2D OI-HPs (**2**, **4**, and **6**). We found that 2D OI-HP:Mn exhibit higher PL-QY without emission-shifting at band-edge emission wavelength than their pure 2D OI-HPs. Notably, these bright fluorescence were stable when immersed in water for a long time, as shown in the video in the Supporting Information. **Table 2** summarizes the recent

progress on Mn-doped perovskites. To our surprise, this work is the first to realize the water stability of Mn-doped perovskites as well as the highest PL-QY of the Mn-doped layered perovskites.

The intriguing performance of our synthesized perovskites is attributed to the free exciton and self-trapped exciton absorptions from $\text{Mn}^{2+} \ ^4\text{T}_1\text{-}^6\text{A}_1$ ligand field transitions which are associated to the partially broken Mn^{2+} spin prohibition and the spin-orbital coupling in simultaneous creation of an exciton-phonon coupling.^[43] The strong perturbation, which is due to the large discrepancy in ionic radius, gives rise to electron-phonon coupling accompanied with self-trapped excitons in deep traps generated in the dopant 2D OI-HP.^[37,44] We also found that the absorption spectra of **1** exhibits stronger absorption features compared to **3** and **5**, which reveals that the proper quantum and dielectric confinement effects can tune the electric properties in Mn-doped perovskite. Herein we ascribe all the differences to a new dual emission mechanism. It occurs due to the quantum and dielectric confinement effects that enhance energy transfer processes between the Mn dopant and semiconductor host, including 1) 2D OI-HP intrinsic band-edge emission, 2) the Mn^{2+} d–d ($^4\text{T}_1$ to $^6\text{A}_1$) spin-forbidden transition, and 3) reabsorption of exciton emission, as shown in Figure 3d.

To further confirm the dual emission processes in layered perovskites, multiphoton confocal fluorescence microscopy and temperature dependent fluorescence spectra measurements were conducted (**Figure 4**; Figures S18 and S19, Supporting Information). Surprisingly, fluorescence microscopy images for **1**, **3**, and **5** showed strong blue emission along with faint orange emission for all disc shaped particles and strong orange luminescence for solid powder (Figure 4a–c). The confocal PL spectra for single crystals showed the corresponding blue and reddish orange emission peaks (Figure 4). The multi-PL of layered perovskites was further observed in 3D multiphoton confocal fluorescence microscopy images (Figures S18 and S19, Supporting Information). The fluorescence microscopy images in channel 1 (410–550 nm) (Figures S18a and S19a, Supporting Information) and channel 2 (551–698 nm) (Figures S18b and S19b, Supporting Information) were obtained to separate the mixture of dual emission. Blue and reddish orange luminescence for **1** and **3** were observed, respectively. The visible light range of fluorescence microscopy image in Figures S18d and S19d (Supporting Information) showed the obviously coincident single particle fluorescence for every nanoplate compared to the microscopy images in Figures S18c and S19c (Supporting Information). These 3D multiphoton

Table 1. Composition analysis and optical properties for Mn-doped 2D perovskite (**1**, **3**, and **5**) and 2D perovskite (**2**, **4**, and **6**).

Sample	Input Mn:Pb (molar ratio)	EDS Pb:Mn (x) (molar ratio)	PL-QY [%]	PL emission peaks	
				Band-edge emission [nm]	Mn^{2+} emission
1	4	1.55	45	416	Centered at 595 nm
2	0	0	12.9	415	No
3	4	0.88	13.3	420	Centered at 600 nm
4	0	0	7.23	421	No
5	4	1.35	9.4	412	Centered at 600 nm
6	0	0	4.11	412	No

Table 2. Summary progresses of selected Mn-doped perovskite nanocrystals for their synthesis features, dimension, water stability, and PL-QY.

Mn-doped perovskites	Synthesis highlight	Water stability	PL-QY	Ref.
Mn-doped CsPbCl ₃	Hot injection	No	58%	[20]
Mn-doped CsPbX ₃	Postsynthetic anion exchange	No	27%	[21]
Mn-doped cubic CH ₃ NH ₃ PbCl ₄	Room-temperature synthesis	No	15%	[52]
Mn-doped 2D (C ₄ H ₉ NH ₃) ₂ PbBr ₄	Solid-state grinding	No	37%	[38]
Mn:L ₂ PbCl ₄ and Mn:CsPbCl ₃	Layered perovskites to doped platelets	No	36%	[23]
Single crystalline Mn:L ₂ PbX ₄	Solution-based synthetic method	No	61%	[24]
Large-sized Mn:(BuA) ₂ PbBr ₄	100 °C synthesis	No	26%	[25]
Mn-doped 2D (PEA) ₂ PbBr ₄	Lewis base–assisted precipitated method	Yes	45%	This work

confocal fluorescence microscopy images provide a further evidence for Mn²⁺ ion dopant in 2D OI-HP lattice because no impurity was shown in the images. The obvious discrepancy between confocal fluorescence images and the luminescence images under UV light is considered to be due to the efficient energy transfer (ET) emission (reddish orange color under UV light) and self-reabsorption back energy transfer (BET) (blue color with faint red color in cofocal fluorescence images), as shown in Figure 3d. When irradiated under UV light, energy transfer dominates the PL. In the case of the multiphoton point excitation with a pulsed laser with 405 nm, Mn²⁺ dopants are activated to high energy and the back energy transfer dominates the PL. The existence of the two luminescent processes are confirmed by the confocal PL spectra (Figure 4d–f) including band-edge emission and Mn²⁺ ⁴T₁–⁶A₁ ligand field transition.

The energy transfer processes are further proven with the temperature dependent PL spectra performed at 298 and 77 K with the excitation wavelength at 350 nm for all samples. (Figure 4h–l; Figure S17, Supporting Information). In contrast to the PL peaks of **1** and **3** at room temperature, an unusual evolution of PL peaks at 77 K shows that Mn²⁺ emission dominates the PL spectra, accompanied with small band-edge emission (Figure 4h–l). At 298 K, strong narrow peak emerges at nearly 415 nm, corresponding to the blue luminescence, while a broad emission peak centers at 600 nm, corresponding to the red luminescence. These phenomena are also shown by confocal fluorescence images (Figures S18 and S19, Supporting Information). Upon decreasing the temperature to 77 K, the peak intensity of blue fluorescence weakens and the peak shifts to a higher energy. Meanwhile, the peak of reddish orange fluorescence shifts to a lower energy and becomes the dominant feature (Figure 4h–l). But, the situation is different for **5**. At low temperatures, no enhanced Mn²⁺ emission peak was observed, but the PL peaks shift with the same trend as in **1** and **3**. We conclude that a strong temperature dependence of exciton PL for **1** and **3** is consistent with a simple model of energy transfer between self-trapped exciton and free exciton states.^[45] At room temperature, the activation-energy barriers which separate free exciton and self-trapped exciton states can easily be overcome and the carriers are thermally detrapped from self-trapped exciton states towards the free exciton state.^[21] The process is illustrated by K_{ET} and K_{BET} processes in Figure 3d. When cooled to 77 K, there is no sufficient thermal energy for the carriers in self-trapped exciton state to surmount the activation energy barrier in order to detrapp back to free exciton state.^[44,45]

As a result, the Mn²⁺ ⁴T₁–⁶A₁ transition emission dominates as a PL feature under 77 K, while the PL spectra mainly exhibit band-edge emission at room temperature (Figure 4d–f).

Furthermore, Pradhan and co-workers^[24] reported that the Mn emission intensity gradually enhanced as the Mn/Pb ratio increased up to a certain level, but then the Mn emission intensity disappeared due to the disintegration of perovskite moiety. We also found a similar situation when we chose different intake ratios of Mn/Pb such as 0.062, 0.125, 1, and 4 and found that the Mn/Pb ratio of 4/1 is optimal (Figure S20, Supporting Information), which indicates that the most efficient energy transfer occurs in the case of Mn/Pb ratio 4/1. This is attributed to the presence of more number of Mn²⁺ centers in **1**, **3**, and **5**. However, the Mn/Pb ratio observed from SEM-EDS analysis is less than that of the optimal Mn/Pb ratio (4/1). This revealed that only a minor amount of Mn ions got inside the crystals despite a large amount of Mn precursor salts in the reaction flask. A similar kind of phenomenon was also observed in previous reports.^[24,46]

2.3. Water Stabilization of Mn-Doped 2D OI-HP and 2D OI-HP

PEA cation and B site dopant ion act a crucial role via coordination in stabilizing the perovskite against water. We found that **3** and **5** crystallized from butylamine (BuA) and benzylamine (BA) decomposed in water quickly, while **1** crystallized from PEA shows bright fluorescence in water, as shown in the video in the Supporting Information. The animation shows that **1** exhibits luminescence with slight abatement under interaction with water, while **3** and **5** decomposed quickly after injecting water into bottle. Previously, Grancini et al. reported that the crystal edge became a more sensitive region to have the first step of hydration process where hydrogen bonding formed spontaneously between water molecules and inorganic layer.^[47] Likewise, further percolation of water into the inner structure of the perovskite lattice depends on water adsorption energy and water diffusion energy along the facet, which are determined by their different termination and polarization.^[47–49] Here we investigated the water-resistance feature of **1**, **3**, and **5**. In the case of Mn-doped 2D perovskite **1**, the hydrophobic organic layer and dopant ion controlled lattice structure led to the best tolerance to water corrosion. The powder HP-XRD (Figure 5) and morphology characterization (Figures S11–S13, Supporting Information) revealed that the structure and

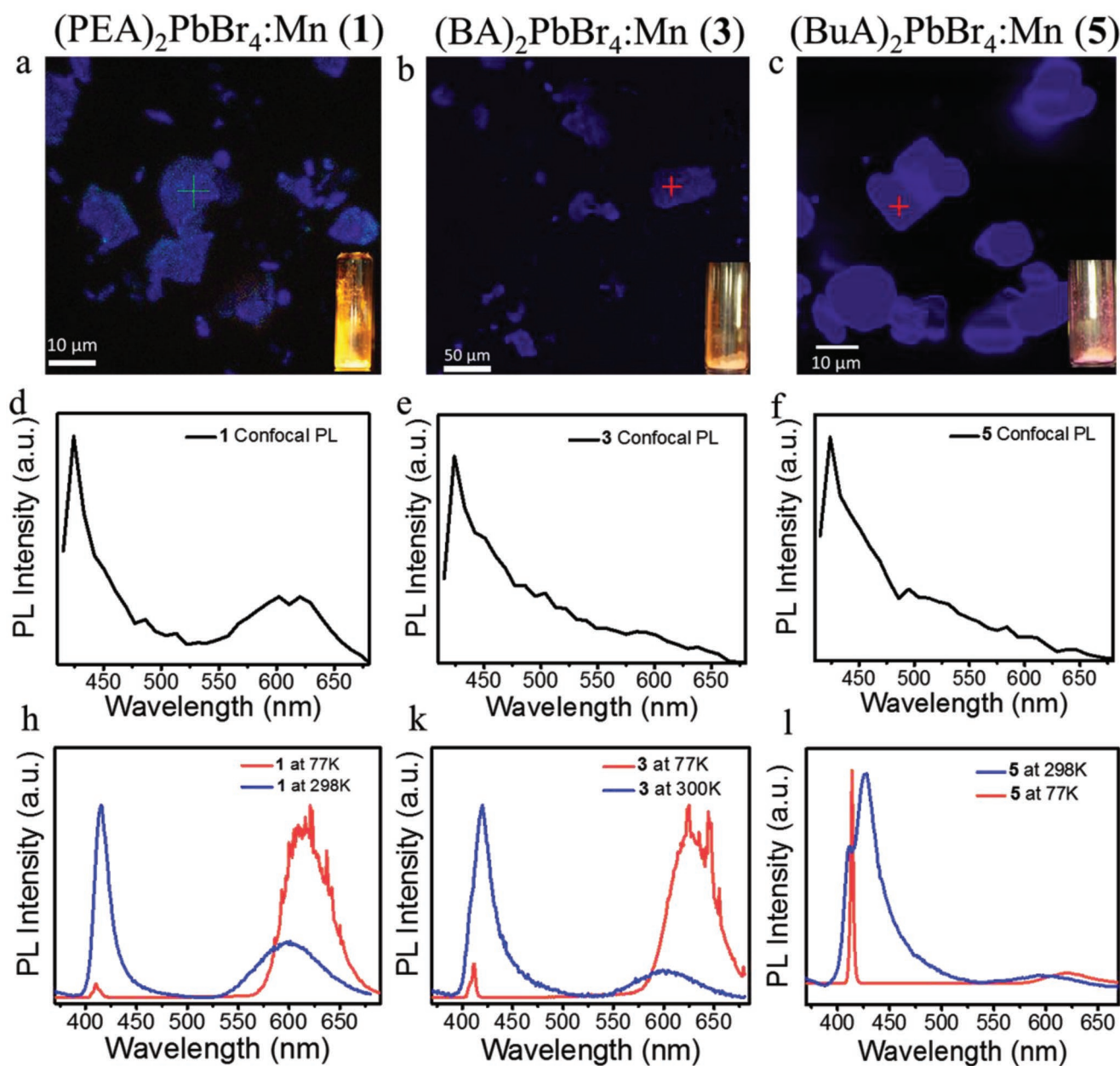


Figure 4. Energy transfer evolution as luminescent changing for compounds 1, 3, and 5. The confocal fluorescence microscopy images and the inset solid luminescent images under 365 nm UV light for a) 1, b) 3, and c) 5, respectively. The confocal PL spectra excited at 405 nm laser for d) 1, e) 3, and f) 5, respectively. The temperature dependence PL spectra at 298 and 77 K excited at 350 nm for h) 1, k) 3, and l) 5, respectively.

morphology of nanoplates 1 retain as they are without interacting with water after immersing in water over 45 days, demonstrating the water-stable layered structure. This was also confirmed from the comparison of XRD patterns before and after immersing 1 in water. The magnified views in different angle range (Figure 5b–e) show the perfect consistency of diffraction angles giving the same oriented crystal structure along the (00l) direction between the two samples before and after immersing 1 in water. To evaluate the stable fluorescence properties in water, we investigated the PL after immersing all the powders in water for 1 h under 365 nm UV light (Figure 6a). The results reveal that only 1 showed the bright luminescence,

while the fluorescence of 3 and 5 vanished soon after injecting water to the bottle (as shown in the video in the Supporting Information).

In Figure 6c, static contact angle tests of glass and PEAP-Mn films with deionized water were performed. After evaluation of the film with three of each type, the average contact angles of the hydrophilicity for glass and PEAP-Mn films were 22.8° and 14.8°, respectively (Figure 6c). In order to strengthen the evidence of the water-stable films, we kept the water drop on the surface of film and glass for 5 min each. The contact angle of water drop on the glass decreases, while that on the surface of the film remained to be same. This is because the hydrophilic

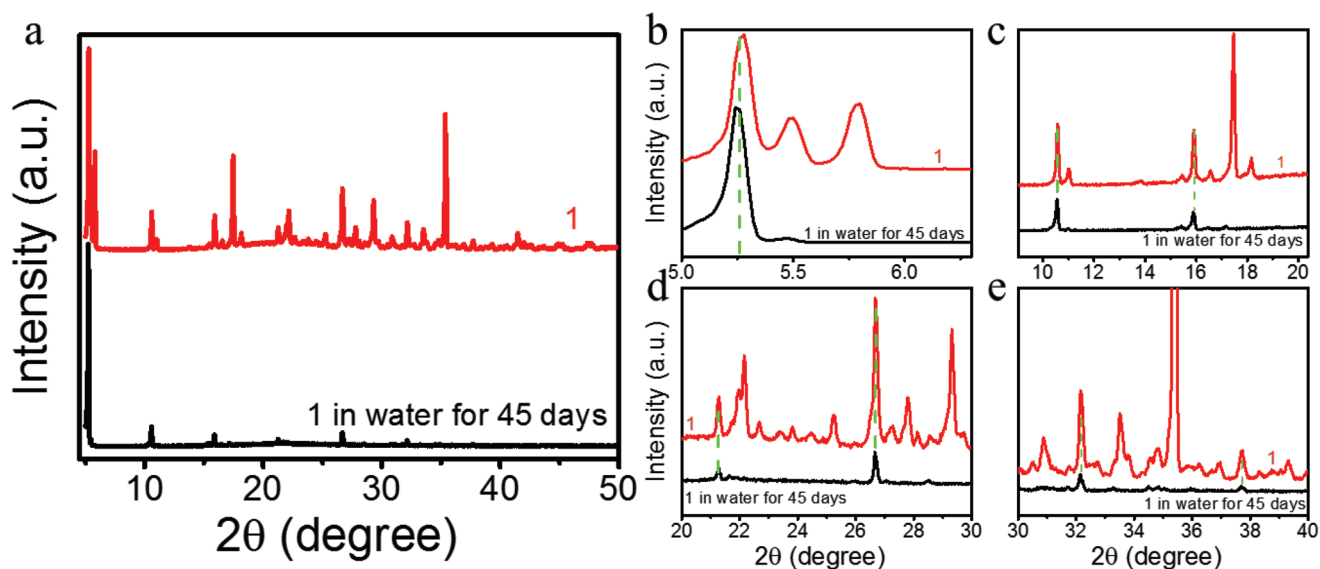


Figure 5. a) XRD patterns of **1** and water immersed **1** for 45 days and their magnified views in the degree range of b) 5°–6.5°, c) 10°–20°, d) 20°–30°, and e) 30°–40°.

feature of glass leads to a change of surface tension. Figure 6c shows a schematic diagram of the mechanism for water-stable properties of perovskite **1**. The hydrophobic molecules in the A site can reduce water adsorption energy and prevent the water ingress into the sublattice of the layered structure. The enhanced formation energy of lattice structure increases the energy barrier for water diffusion into inner structure which degrades crystals. The steric arrangement of the PEA functional

molecules terminated on surface of perovskite inorganic layer results in high surface absorption energy, which induces a water-resistance layer.^[13] The substitution of Pb^{2+} ions (ionic radius = 1.33 Å) with smaller Mn^{2+} ions (ionic radius = 0.97 Å) will also help in shrinking the lattice cell and enhance the formation energy of the perovskite lattice cell.^[21] As a result, **1** shows a distinctive water repelling ability, as shown in the video in the Supporting Information and Figure 6.

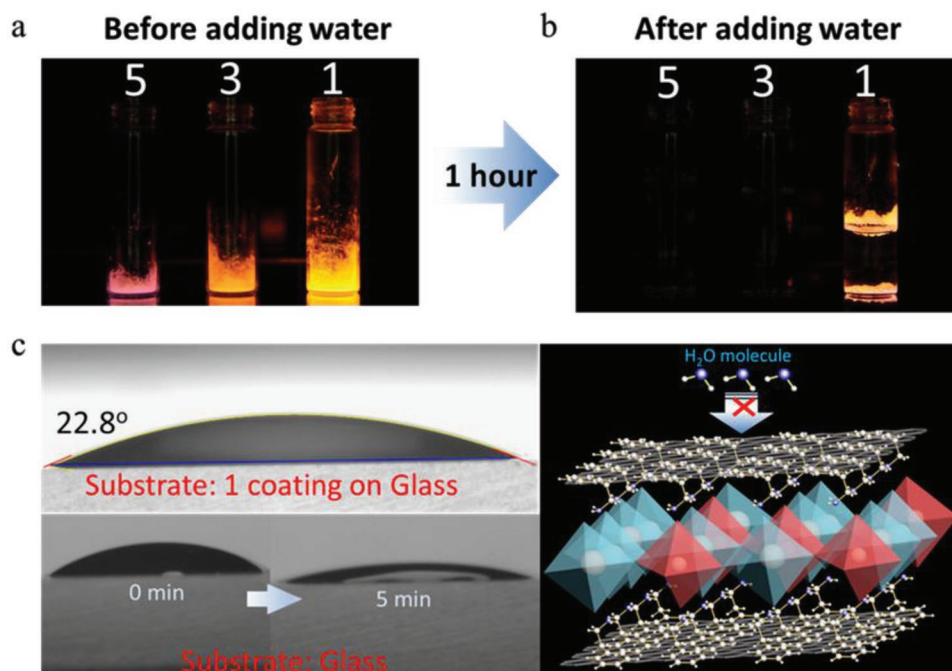


Figure 6. Water-stable fluorescence performance. a) The solid luminescence images under 365 nm UV light, b) the fluorescence images after immersing in water for 1 h for **5**, **3**, **1**, and c) schematic of plausible water-resistance mechanism and water static contact angles for $(\text{PEA})_2\text{PbBr}_4\text{:Mn}$ (PEAP-Mn) coated on glass and glass.

For practical applications, the thin films with smooth surface and the nanoparticles dispersed in solution are more attractive. Zeng and co-workers make an important contribution to developing high quality films of perovskite in LED application.^[50,51] We also transferred the water-stable perovskite powder to the film. We successfully fabricated the film on etched glass surface and took the luminescent images of film under 365 nm UV lamp (Figure S22, Supporting Information). The film conditions are shown in Figure S22b,d (Supporting Information). At the present status we are in the process of optimizing the film quality for use of devices.

3. Conclusion

We have developed a simple yet cost-efficient acid solution-assisted precipitation method to synthesize highly water-stable 2D OI-HPs through Mn²⁺ doping. They show excellent fluorescence properties with dual emission including Mn²⁺ d-d transition and intrinsic semiconductor band-edge emission. The dual emission of these Mn-doped perovskites was investigated carefully by optical and multiphoton confocal fluorescence microscopy. We found that the diverse energy transfer processes between host semiconductor and dopant are attributed to the quantum and dielectric confinement effects. Out of the three amino group containing molecules, BuA, BA, and PEA, only 1 shows PL-QY exceeding 45% and stable fluorescence in water over 45 days. Through contact angles and solid-state luminescence tests in water, we ascribed the long-term water stability of (PEA)₂PbBr₄:Mn to the highly hydrophobic PEA molecule matching well with the distorted structure of Mn-doped 2D OI-HP. As a result, the increased water resistance and the enhanced formation energy of the lattice cell cooperate to achieve long-term water stability. These findings will help in exploring useful mechanisms to fabricate water-stable metal-doped 2D OI-HPs and understanding dual emission principles, which are critical for advancing the materials development toward highly luminescence-efficient perovskite LEDs.

4. Experimental Section

General Experimental Procedure for Compounds 1, 3, and 5: Lead bromide (0.184 g, 0.5 mmol) and manganese bromide (0.43 g, 2 mmol) were dissolved in acid solution (2 mL) in a 25 mL one-neck bottle, followed by slow addition of amine (5 mmol) to a vial under vigorous stirring. The pH of the solution remained highly acidic. The precipitate was filtered and washed with ether and finally dried at 60 °C in oven.

General Experimental Procedure for Compounds 2, 4, and 6: Lead bromide (PbBr₂) (0.367 g, 1 mmol) was dissolved in acid solution (2 mL) in a 25 mL one-neck bottle, followed by slow addition of amine (2 mmol) to a vial under vigorous stirring. The pH of the solution remained highly acidic. The precipitate was filtered and washed with ether and finally dried at 60 °C in oven.

General Procedure to Fabricated Perovskite Film 1: Powder 1 was dispersed in solution of DMF and toluene under vigorous stirring. The precursor solution was spin-casted on the etched glass (1.5 cm × 1.5 cm) to obtain perovskite film after evaporating the solvent.

Supporting Information

Supporting Information is available from the Wiley Online Library or from the author.

Acknowledgements

Q.B. and A.J. contributed equally to this work. This work was supported by NRF (National Honor Scientist Program: 2010-0020414).

Conflict of Interest

The authors declare no conflict of interest.

Keywords

2D perovskites, dual emission, Mn dopant, water-stable perovskites

Received: June 14, 2019

Revised: July 23, 2019

Published online:

- [1] S.-R. Bae, Q. Van Le, S.-Y. Kim, *Small Methods* **2019**, *21*, 24.
- [2] A. R. Bin Mohammad Yusoff, M. K. Nazeeruddin, *Adv. Energy Mater.* **2018**, *8*, 1.
- [3] Y. Wei, Z. Cheng, J. Lin, *Chem. Soc. Rev.* **2019**, *48*, 310.
- [4] K. Lin, J. Xing, L. N. Quan, F. P. G. de Arquer, X. Gong, J. Lu, L. Xie, W. Zhao, D. Zhang, C. Yan, W. Li, X. Liu, Y. Lu, J. Kirman, E. H. Sargent, Q. Xiong, Z. Wei, *Nature* **2018**, *562*, 245.
- [5] Y. H. Kim, H. Cho, J. H. Heo, T. S. Kim, N. S. Myoung, C. L. Lee, S. H. Im, T. W. Lee, *Adv. Mater.* **2015**, *27*, 1248.
- [6] L. Zhao, K. M. Lee, K. Roh, S. U. Z. Khan, B. P. Rand, *Adv. Mater.* **2019**, *31*, 1.
- [7] H. Tsai, W. Nie, J. C. Blancon, C. C. Stoumpos, C. M. M. Soe, J. Yoo, J. Crochet, S. Tretiak, J. Even, A. Sadhanala, G. Azzellino, R. Brenes, P. M. Ajayan, V. Bulović, S. D. Stranks, R. H. Friend, M. G. Kanatzidis, A. D. Mohite, *Adv. Mater.* **2018**, *30*, 1704217.
- [8] H. Tsai, W. Nie, J. C. Blancon, C. C. Stoumpos, R. Asadpour, B. Harutyunyan, A. J. Neukirch, R. Verduzco, J. J. Crochet, S. Tretiak, L. Pedesseau, J. Even, M. A. Alam, G. Gupta, J. Lou, P. M. Ajayan, M. J. Bedzyk, M. G. Kanatzidis, A. D. Mohite, *Nature* **2016**, *536*, 312.
- [9] H. Cho, S.-H. Jeong, M.-H. Park, Y.-H. Kim, C. Wolf, C.-L. Lee, J. H. Heo, A. Sadhanala, N. Myoung, S. Yoo, S. H. Im, R. H. Friend, T.-W. Lee, *Science* **2015**, *350*, 1222.
- [10] A. Jana, M. Mittal, A. Singla, S. Sapra, *Chem. Commun.* **2017**, *53*, 3046.
- [11] X. Yang, X. Zhang, J. Deng, Z. Chu, Q. Jiang, J. Meng, P. Wang, L. Zhang, Z. Yin, J. You, *Nat. Commun.* **2018**, *9*, 2.
- [12] K. K. Bass, R. E. McAnally, S. Zhou, P. I. Djurovich, M. E. Thompson, B. C. Melot, *Chem. Commun.* **2014**, *50*, 15819.
- [13] F. Wang, W. Geng, Y. Zhou, H. H. Fang, C. J. Tong, M. A. Loi, L. M. Liu, N. Zhao, *Adv. Mater.* **2016**, *28*, 9986.
- [14] I. C. Smith, E. T. Hoke, D. Solis-Ibarra, M. D. McGehee, H. I. Karunadasa, *Angew. Chem., Int. Ed.* **2014**, *53*, 11232.
- [15] L. N. Quan, M. Yuan, R. Comin, O. Voznyy, E. M. Bearegard, S. Hoogland, A. Buin, A. R. Kirmani, K. Zhao, A. Amassian, D. H. Kim, E. H. Sargent, *J. Am. Chem. Soc.* **2016**, *138*, 2649.
- [16] Q. Jiang, D. Rebolgar, J. Gong, E. L. Piacentino, C. Zheng, T. Xu, *Angew. Chem., Int. Ed.* **2015**, *54*, 7617.

- [17] Q. Tai, P. You, H. Sang, Z. Liu, C. Hu, H. L. W. Chan, F. Yan, *Nat. Commun.* **2016**, 7, 1.
- [18] A. Jana, K. S. Kim, *ACS Appl. Energy Mater.* **2019**, 2, 4496.
- [19] A. Jana, K. S. Kim, *ACS Energy Lett.* **2018**, 3, 2120.
- [20] D. Parobek, B. J. Roman, Y. Dong, H. Jin, E. Lee, M. Sheldon, D. H. Son, *Nano Lett.* **2016**, 16, 7376.
- [21] W. Liu, Q. Lin, H. Li, K. Wu, I. Robel, J. M. Pietryga, V. I. Klimov, *J. Am. Chem. Soc.* **2016**, 138, 14954.
- [22] S. Zou, Y. Liu, J. Li, C. Liu, R. Feng, F. Jiang, Y. Li, J. Song, H. Zeng, M. Hong, X. Chen, *J. Am. Chem. Soc.* **2017**, 139, 11443.
- [23] S. Das Adhikari, A. Dutta, S. K. Dutta, N. Pradhan, *ACS Energy Lett.* **2018**, 3, 1247.
- [24] S. K. Dutta, A. Dutta, S. Das Adhikari, N. Pradhan, *ACS Energy Lett.* **2019**, 4, 343.
- [25] T. Sheikh, A. Nag, *J. Phys. Chem. C* **2019**, 123, 9420.
- [26] A. Jana, Q. Ba, K. S. Kim, *Adv. Funct. Mater.* **2019**, 29, 1900966.
- [27] G. Pan, X. Bai, D. Yang, X. Chen, P. Jing, S. Qu, L. Zhang, D. Zhou, J. Zhu, W. Xu, B. Dong, H. Song, *Nano Lett.* **2017**, 17, 8005.
- [28] N. Kitazawa, Y. Watanabe, *J. Phys. Chem. Solids* **2010**, 71, 797.
- [29] K. Gauthron, J. Lauret, L. Doyennette, G. Lanty, A. Al Choueiry, S. J. Zhang, L. Largeau, O. Mauguin, J. Bloch, E. Deleporte, *Opt. Express* **2010**, 18, 5912.
- [30] N. Kitazawa, *Mater. Sci. Eng., B* **1997**, 49, 233.
- [31] L. Dou, A. B. Wong, Y. Yu, M. Lai, N. Kornienko, S. W. Eaton, A. Fu, C. G. Bischak, J. Ma, T. Ding, N. S. Ginsberg, L.-W. Wang, P. Alivisatos, P. Yang, *Science* **2015**, 349, 1518.
- [32] D. Liang, Y. Peng, Y. Fu, M. J. Shearer, J. Zhang, J. Zhai, Y. Zhang, R. J. Hamers, T. L. Andrew, S. Jin, *ACS Nano* **2016**, 10, 6897.
- [33] A. K. Guria, S. K. Dutta, S. Das Adhikari, N. Pradhan, *ACS Energy Lett.* **2017**, 2, 1014.
- [34] M. H. P. Usman, R. Bakthavatsalam, J. Kundu, *ChemistrySelect* **2018**, 3, 6585.
- [35] P. I. Archer, X. Liu, S. Lee, G. M. Salley, M. Dobrowolska, J. K. Furdyna, D. R. Gamelin, *Nano Lett.* **2008**, 8, 1197.
- [36] P. I. Archer, S. A. Santangelo, D. R. Gamelin, *J. Am. Chem. Soc.* **2007**, 129, 9808.
- [37] R. Beaulac, P. I. Archer, J. Van Rijssel, A. Meijerink, D. R. Gamelin, *Nano Lett.* **2008**, 8, 2949.
- [38] A. Biswas, R. Bakthavatsalam, J. Kundu, *Chem. Mater.* **2017**, 29, 7816.
- [39] K. Xu, A. Meijerink, *Chem. Mater.* **2018**, 30, 5346.
- [40] C. C. Stoumpos, D. H. Cao, D. J. Clark, J. Young, J. M. Rondinelli, J. I. Jang, J. T. Hupp, M. G. Kanatzidis, *Chem. Mater.* **2016**, 28, 2852.
- [41] X. Hong, T. Ishihara, A. V. Nurmikko, *Phys. Rev. B* **1992**, 45, 6961.
- [42] T. Ishihara, J. Takahashi, T. Goto, *Solid State Commun.* **1989**, 69, 933.
- [43] U. Kambli, H. U. Gudel, B. Briat, *J. Phys. C: Solid State Phys.* **1984**, 17, 3113.
- [44] X. Wu, M. T. Trinh, D. Niesner, H. Zhu, Z. Norman, J. S. Owen, O. Yaffe, B. J. Kudisch, X.-Y. Zhu, *J. Am. Chem. Soc.* **2015**, 137, 2089.
- [45] M. D. Smith, A. Jaffe, E. R. Dohner, A. M. Lindenberg, H. I. Karunadasa, *Chem. Sci.* **2017**, 8, 4497.
- [46] A. De, N. Mondal, A. Samanta, *Nanoscale* **2017**, 9, 16722.
- [47] G. Grancini, V. D'Innocenzo, E. R. Dohner, N. Martino, A. R. Srimath, G. Grancini, V. D'Innocenzo, E. R. Dohner, N. Martino, A. R. Srimath Kandada, E. Mosconi, F. De Angelis, H. I. Karunadasa, E. T. Hoke, A. Petrozza, *Chem. Sci.* **2015**, 6, 7305.
- [48] N. Z. Koocher, D. Saldana-Greco, F. Wang, S. Liu, A. M. Rappe, *J. Phys. Chem. Lett.* **2015**, 6, 4371.
- [49] L.-M. L. Chuan-Jia Tong, W. Geng, Z.-K. Tang, C.-Y. Yam, X.-L. Fan, J. Liu, W.-M. Lau, *J. Phys. Chem. Lett.* **2015**, 6, 3289.
- [50] X. Li, Y. Wu, S. Zhang, B. Cai, Y. Gu, J. Song, H. Zeng, *Adv. Funct. Mater.* **2016**, 26, 2435.
- [51] Y. Wang, X. Li, J. Song, L. Xiao, H. Zeng, H. Sun, *Adv. Mater.* **2015**, 27, 7101.
- [52] X. Li, Y. Guo, B. Luo, *Crystals* **2017**, 8, 4.